Optical transmission and dimensional stability of single-crystal sapphire after high-dose neutron irradiation at various temperatures up to 688°C*

Christian M. Petrie[1,a], Anthony Birri[b], Thomas E. Blue[b]

[a] Oak Ridge National Laboratory, P.O. Box 2008, Oak Ridge, TN, USA, 37831

[b] The Ohio State University, 281 W. Lane Ave., Columbus, OH, USA, 43210

Abstract

The use of single-crystal sapphire optical fibers has been considered to extend fiber-optic sensing to the extreme temperature (>1000°C) environments encountered in nuclear applications. However, before these sapphire fiber–based sensors can be deployed, their optical transmission and dimensional stability (which impacts drift of some sensors) must be characterized under representative testing conditions. Data regarding the optical transmission of sapphire following high-dose neutron irradiation at temperatures >100°C is extremely limited. This work provides measurements of optical density (i.e., attenuation) and directional dimensional changes in bulk single-crystal sapphire materials irradiated to a fast neutron fluence of 2.4×10^{21} n/cm^2 (3.5 displacements per atom) at temperatures ranging from 95 to 688°C. Optical density measured after irradiation at 95 and 298°C showed ultraviolet and visible absorption bands corresponding to known defect centers and temperature trends that were generally consistent

[1] Corresponding author: petriecm@ornl.gov

with previous ex situ and in situ measurements made at much lower neutron fluence. However, optical density measured after irradiation at 688°C was as much as two orders of magnitude higher, indicating that the fundamental mechanism for radiation-induced attenuation changes at this irradiation temperature. Additional analysis and comparison with previous works suggest that the attenuation may result from void formation, leading to increased Rayleigh scattering losses in the material and increased swelling that would also result in drift of Bragg grating-based sensors in sapphire fibers. These results pose serious questions regarding the feasibility of sapphire fiber–based sensors for high-temperature nuclear applications.

Keywords: Radiation; fiber-optic; transmission; dimensional change; sapphire; optical

1. Introduction

The nuclear industry has pursued development of advanced high-temperature reactors for many decades because of their increased thermal efficiency, uranium utilization, and passive safety, as well as their potential to provide high-temperature process heat and burnup of minor actinides. For example, high-temperature gas-cooled reactors use a high pressure (~7 MPa) helium coolant with core outlet temperatures as high as 1000°C [1-3]. Molten salt–cooled reactors have been considered, with solid fuels or dissolved liquid fuels operating at temperatures up to 800°C or higher [4, 5]. Considerable efforts have been made to develop materials capable of surviving the combination of high temperatures, high pressures, radiation damage, and chemically aggressive media [6], but less focus has been placed on in-core sensors that must survive the same conditions while providing adequate signal strength with minimal drift over a period of months to years [7, 8]. While some reactor instrumentation can be located outside the core, the ability to monitor temperature distributions within the coolant, fuel, and structural materials would greatly improve the understanding of limiting design- and safety-related core locations to inform both reactor designers and operators [9]. Furthermore, monitoring of fuel temperatures during irradiation in test reactors is critical to proving their safety and qualifying new fuels for light water or advanced reactors [10-12].

Fiber-optic sensors are one candidate technology for in-core instrumentation in advanced reactors or irradiation experiments in tests reactors due to their small size, immunity to electromagnetic interference, and ability to measure a wide range of parameters, some of which include spatially-distributed measurements. For example, fiber-optic–based sensors have been used to measure pressure [13-15], flow [16-18], and liquid level [19-21], as well as low doses of neutron and gamma radiation [22-24]. Distributed temperature and strain measurements have

been demonstrated using traditional fused silica fibers at temperatures as high as ~1000°C [25-27] and ~500°C [28-30], respectively. However, for temperatures beyond ~1000°C, fused silica-based optical fibers suffer from devitrification [31], which limits long-term use at these temperatures.

For applications with temperatures >1000°C, single-crystal sapphire optical fibers have shown promise. Sapphire-based fibers must be single crystalline to limit scattering losses that would otherwise be introduced at grain boundaries, which can limit the minimum fiber diameter and maximum fiber length that can be grown. Due to technical challenges associated with developing a thermally stable, high-temperature cladding for sapphire fibers, these fibers are often air-clad. The large diameter and lack of cladding makes sapphire fibers highly multimodal and sensitive to diameter non-uniformities, resulting in significant radiative optical losses [32]. Methods for creating high-temperature sapphire fiber claddings have been demonstrated using chemical dopants [33-35] and displacement damage from charged particles [36, 37]. The use of polycrystalline alumina and other ceramic materials have also been proposed [38, 39]. Although unclad sapphire fibers suffer from prohibitive attenuation in air at 1400°C [40], operating the fiber in an inert environment can ameliorate these effects [41]. Despite these challenges, it is possible to conduct distributed temperature sensing using Bragg gratings in sapphire fibers, as evidenced by previous works that measured temperatures as high as 1500°C using these gratings [42-45].

In order to extend high-temperature sapphire fiber–based sensors to nuclear applications, the fibers must have manageable radiation-induced attenuation (RIA) of the light signal due to color center formation during exposure to ionizing radiation. Radiation-induced dimensional changes also impact sapphire fiber–based sensors in the form of signal drift that cannot be

separated from changes in temperature. This paper provides new information regarding the feasibility of operating sapphire fiber–based sensors in high-temperature nuclear applications by evaluating changes in optical transmission and dimensional stability after high dose neutron irradiation at various temperatures.

1.1. Radiation-induced attenuation

Because of the relatively recent commercialization of single-crystal sapphire optical fibers, significantly less work has been devoted to developing radiation-hard sapphire optical fibers compared to their fused silica counterparts. Previous measurements of RIA in sapphire optical fibers from both neutrons and gamma rays have generally shown significant growth in point defect absorption in the ultraviolet (UV)-to-visible range that extends into the near infrared range [46-50]. Irradiation with gamma rays showed a saturation of the RIA [47], whereas irradiation with neutrons resulted in linear increases in RIA that did not show any signs of approaching saturation up to a maximum fast neutron fluence of 1.4×10^{16} n/cm^2 [48]. Increasing temperature up to 1000°C during irradiation resulted in monotonic reductions in the equilibrium gamma ray RIA [47] and monotonic decreases in the rate of increase in RIA during neutron irradiation [49]. Similar decreases in neutron RIA were observed with increasing temperature from cryogenic temperatures to room temperature [51].

RIA in sapphire has also been measured using “bulk” slab or disk geometries. Early studies focused on the identification of the fundamental optical absorption bands that form following irradiation with gamma rays, ions, or low fluences (10^{18} n/cm^2 or lower) of neutrons [52-54], as well as their high-temperature annealing behaviors [55-57]. Later studies tested samples irradiated to higher fast neutron fluences on the order of 10^{19} to 10^{20} n/cm^2 [58-61]. However, nearly all previous RIA measurements of bulk Al_2O_3 were performed following

irradiation at temperatures <100°C. Pells reported the optical density of sapphire samples following neutron irradiation to 3×10^{19} n/cm^2 at temperatures up to 290°C, but the optical density was only reported at a single wavelength [61]. The spectral features of the RIA observed previously in bulk samples were largely similar to those of the RIA observed in sapphire fibers, with absorption peaks located in the UV-to-visible range that extend into the near-infrared range. Post-irradiation thermal annealing of the RIA showed significant reductions in absorption, particularly when the annealing temperature exceeded 400°C [56, 59]. These results are consistent with previous in situ measurements showing the largest reduction in RIA occurring as the irradiation temperature was increased from 300 to 600°C [49]. Still, there are no data available regarding high-dose (on the order of 1 displacement per atom, or dpa) neutron irradiation effects on RIA in sapphire at temperatures >100°C.

1.2. Radiation-induced swelling

Displacement damage cascades from neutron radiation are known to generate point defects (vacancies and interstitials) that can eventually aggregate and form defect clusters such as dislocations or voids [62]. The evolution of these microstructural defects is complex, and depends on the crystal structure, dose, and defect mobility (i.e., temperature), among other parameters. The most obvious neutron radiation effect on single-crystal sapphire fibers is the increased RIA (discussed in Section 1.1) resulting from trapping states that are created within the bandgap due to point defects [54]. However, some sapphire fiber-based sensors are also susceptible to signal drift that results from radiation-induced microstructural defects that cause dimensional changes that cannot easily be distinguished from changes in the measurand (i.e., temperature or strain). Diffraction-based techniques can be used to evaluate contributions to the net macroscopic dimensional change from simple lattice expansions caused by point defects and

small defect clusters. However, larger defect clusters such as voids and dislocations also contribute to macroscopic dimensional changes and these contributions cannot be measured using diffraction-based techniques.

During irradiation of α-Al_2O_3 to neutron fluences up to ~3×10^{20} n/cm^2, at temperatures below ~100°C, lattice expansion is isotropic and the volumetric swelling calculated from lattice expansion is essentially equal to that calculated from macroscopic dimensional changes [63]. With increasing dose and temperature, mobile interstitials have been shown to cluster into dislocation loops that form on the basal planes, resulting in anisotropic macroscopic dimensional changes [64, 65]. Because these basal loops unfault with continued irradiation via shearing across the loop plane, they continue to grow until they intersect to form dislocation networks that maintain the same Burgers vector [66, 67], thus providing an unsaturable sink for interstitials and maintaining the increase in anisotropic dimensional changes. Interstitial trapping within the dislocation network also provides an excess of vacancies that can agglomerate into voids [68, 69], resulting in increased macroscopic dimensional expansion due to void swelling. Because voids have been shown to align in rows along the c-axis [68], contributions to macroscopic dimensional changes due to void swelling further increase the swelling anisotropy.

The magnitude of the volumetric radiation-induced swelling does not appear to saturate for a fast neutron fluence as high as 6.9×10^{22} n/cm^2 (Figure 1) [63, 68, 70-74]. Figure 1 only shows data obtained from single-crystalline samples due to the potential for grain separation that can influence the swelling behavior of polycrystalline Al_2O_3 as a result of the significant anisotropy in the observed swelling [71, 75, 76]. Additional data regarding the directionally dependent macroscopic dimensional changes as a function of fast neutron fluence and

temperature are required to provide a more comprehensive evaluation of the potential swelling-induced drift of sapphire optical fiber-based sensors.

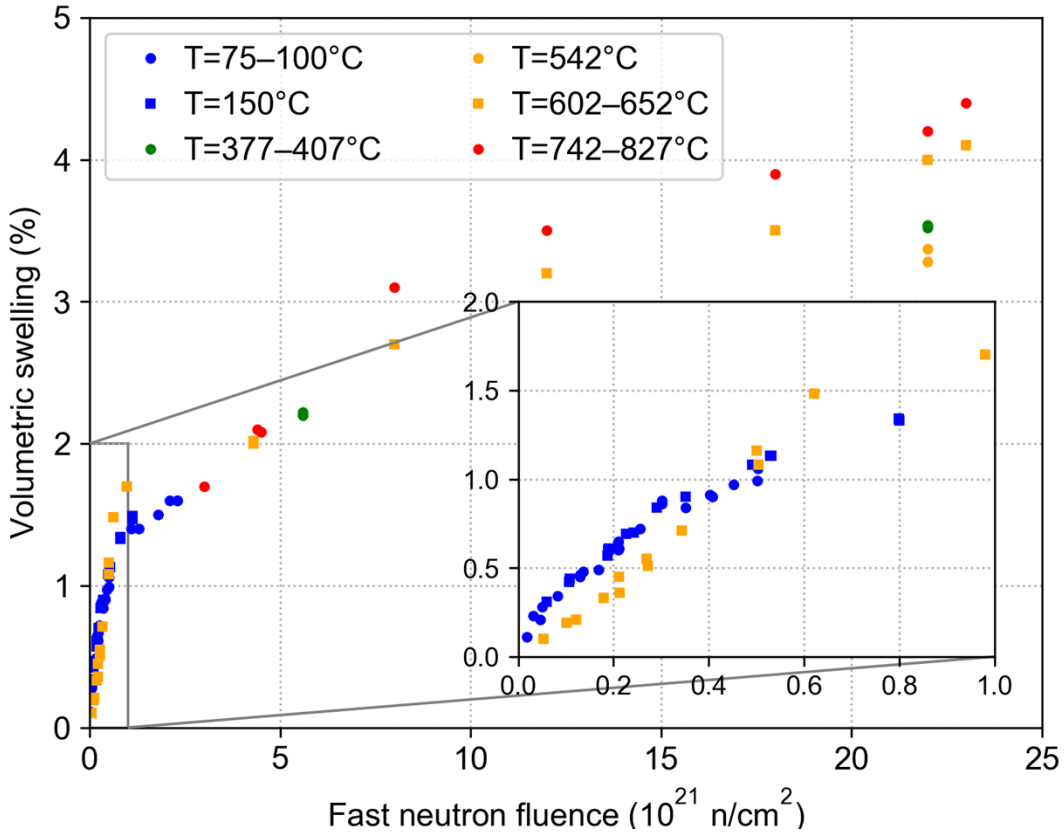

Figure 1. Volumetric swelling vs. fast neutron fluence for single crystal sapphire at various temperatures obtained from the literature [63, 68, 70-74].

1.3. Scope of this paper

This paper provides the first known measurements of broadband RIA in sapphire samples exposed to high-dose (3.5 dpa) neutron irradiation at temperatures above 100°C. Temperature-dependent measurements of directional lattice expansion and macroscopic dimensional change are also reported for single-crystal sapphire samples irradiated to fast neutron fluences (2.4×10^{21} n/cm^2) in between those previously reported by Wilks (6×10^{20} n/cm^2) [70] and Roof and

Ranken (5.6×10^{21} n/cm^2) [74]. The objective of this research is to improve the fundamental understanding of radiation effects on α-Al_2O_3 to determine the suitability of single-crystal sapphire fiber-optic sensors for high-temperature nuclear applications.

2. Experimental methodology

2.1. Samples and irradiation testing

Single-crystal sapphire samples were obtained from Kyocera with the c-axis oriented in the thickness direction. The samples were nominally 16 mm long × 5 mm wide × 0.85 mm thick, with the optical transmission measured through the thickness. The pre-irradiation density was measured to be 3.912 ± 0.016 g/cm^3. Samples were irradiated in "rabbit" capsules in the flux trap of the High Flux Isotope Reactor (HFIR) [77, 78] with an average thermal (neutron energy < 0.5 eV) neutron flux of 1.9×10^{15} n/cm^2/s and an average fast (neutron energy > 0.1 MeV) neutron flux of 1.1×10^{15} n/cm^2/s. The samples were irradiated for 25.7 effective full power (85 MW) days, resulting in thermal and fast neutron fluences of 4.2×10^{21} and 2.4×10^{21} n/cm^2, respectively. The calculated displacement damage is 3.5 dpa using values of 20 and 50 eV for the displacement threshold energies of Al and O, respectively [79]. Three capsules were irradiated, each containing four samples. The average sample temperatures in each of the capsules were previously determined to be 95±8, 298±30, and 688±6°C [80] based on the combination of thermal finite element simulations and post-irradiation dilatometric analyses [81] of passive silicon carbide temperature monitors that were located inside the capsules.

The samples were in contact with a V-4Cr4Ti holder during the irradiation. Therefore, energy dispersive x-ray spectroscopy (EDS) measurements were performed to look for evidence of V [82, 83], Cr [84], and Ti [85] impurities, which can affect the optical transmission in

sapphire. Results showed that V, Cr, and Ti concentrations for all irradiated and virgin samples were indistinguishable from background within the experimental detection limits (~0.5 at%).

2.2. Dimensional and optical transmission measurement

The capsules were cut open in a hot cell post-irradiation. The samples were extracted, cleaned, and transferred to a separate facility where they could be handled using more delicate instruments. Dimensional inspection was performed to measure the sample lengths (a-axis orientation) before and after irradiation using a micrometer to determine radiation-induced dimensional changes. Post-irradiation measurements of sample thickness were also performed to determine optical density (OD) per unit thickness. However, because the thickness was considerably smaller than the length, accurate measurements of the c-axis dimensional changes could not be made.

The samples were then interrogated using a broadband (190−1700 nm) optical transmission system that uses both deuterium (StellarNet SL3) and tungsten halogen (StellarNet SL1) light sources, a custom sample holder, and a pair of spectrometers: a StellarNet SILVER-Nova with a 190−1100 nm range and a StellarNet DWARF-Star with a 900−1700 nm range. The spectrometers were used to determine the wavelength-dependent changes in light intensity for each sample before and after irradiation. Measurements were first made without a sample inserted into the sample holder (the reference scan), and then they were repeated with a sample inserted (the active scan). The RIA in the sample was determined as an OD (in units of cm^{-1}), which is calculated as shown in Eq. (1):

$$\mathrm{OD(E)} = -\frac{1}{\mathrm{L}}\log_{10}\left(\frac{\mathrm{I_A(E)}}{\mathrm{I_R(E)}}\right), \quad (1)$$

where L is the transmission length (equal to the sample thickness), and I_A and I_R are the intensities for the active and reference scans, respectively, as a function of photon energy $E = \frac{hc}{\lambda}$ (where h and c are Planck's constant and the speed of light, respectively), or alternatively, wavelength λ. OD measurements in units of cm^{-1} can be converted to dB/cm (more commonly used for optical fiber geometries) by multiplying by a factor of 10. More details regarding the measurement system and the processing of the optical intensity data are provided in a previous paper [80].

2.3. X-ray diffraction

X-ray diffraction (XRD) was performed on the irradiated samples to determine changes in lattice constants resulting from radiation-induced swelling. Because of radiation and contamination concerns, the only instrument that could handle these samples was a PANalytical X'Pert Pro powder diffractometer that uses a Cu Kα source. This diffractometer could only accommodate the samples when they were oriented with the c-axis (sample thickness) aligned with the x-ray beam. Therefore, only changes in the c-axis lattice parameter could be measured. As mentioned previously, XRD analysis can quantify changes in lattice parameters, but it does not capture the effects of larger defect clusters, such as voids or dislocations, that can affect macroscopic dimensions.

3. Results

3.1. Radiation-induced swelling

Table 1 summarizes macroscopic dimensional changes (a-axis) and changes in the c-axis lattice parameter relative to pre-irradiation values. XRD measurements could not be obtained for two specimens because no peak was observed in the recorded spectra, likely due to sample alignment issues. The magnitude of the a-axis dimensional changes decreased with increasing

irradiation temperature from 95 to 298°C, but it increased with increasing irradiation temperature from 298 to 688°C. The c-axis lattice expansion monotonically decreased with increasing irradiation temperature for all irradiation temperatures and was essentially zero after irradiation at 688°C (i.e., the c-axis lattice parameter did not change relative to its pre-irradiation value). Although this may be coincidental, the measured a-axis dimensional change and c-axis lattice expansion were equal to within experimental uncertainties after irradiation at both 95 and 298°C.

Table 1. Summary of changes in macroscopic dimensions (a-axis) and lattice parameters (c-axis) before and after neutron irradiation to a fast neutron fluence of 2.4×10^{21} n/cm^2.

Irradiation temperature	a-axis macroscopic dimensional change		c-axis lattice expansion	
	Value	Average [standard deviation]	Value	Average [standard deviation]
95°C	0.45%	0.48% [0.03%]	0.42%	0.45% [0.06%]
	0.48%		0.52%	
	0.50%		0.41%	
	0.53%		N/A	
298°C	0.43%	0.41% [0.02%]	0.43%	0.41% [0.04%]
	0.46%		N/A	
	0.39%		0.44%	
	0.40%		0.37%	
688°C	0.64%	0.63% [0.04%]	-0.02%	0.01% [0.03%]
	0.57%		0.05%	
	0.64%		0.04%	
	0.65%		-0.01%	

3.2. Optical transmission

Figure 2 shows OD as a function of photon wavelength for virgin and irradiated samples, with irradiation temperature (T) as a parameter. These OD values were consistent across each of the four samples that were irradiated at each temperature. Increasing the irradiation temperature from 95 to 298°C resulted in an increase in OD over all photon wavelengths <570 nm (energies >2.18 eV). The spectral features of the OD are generally similar after irradiation at temperatures of 95 and 298°C. Increasing the irradiation temperature from 298 to 688°C resulted in large increases in OD. The OD after irradiation at 688°C shows new peaks near 822 nm (1.5 eV) and 587 nm (2.1 eV) that were not present after irradiation at temperatures of 95 and 298°C. For photon wavelengths <410 nm (energies >3 eV), some spectral features of the OD may be similar after irradiation at 688°C vs. after irradiation at 95 and 298°C, although it is difficult to say for certain due to the large uncertainties in the measurements made after irradiation at 688°C. It is also worth mentioning that, even for the measurements made after irradiation at 95 and 298°C,

the optical densities measured in the sapphire samples were significantly greater at all measured wavelengths when compared to those previously measured in amorphous SiO_2 samples irradiated under the same conditions (temperature and neutron fluence) [80].

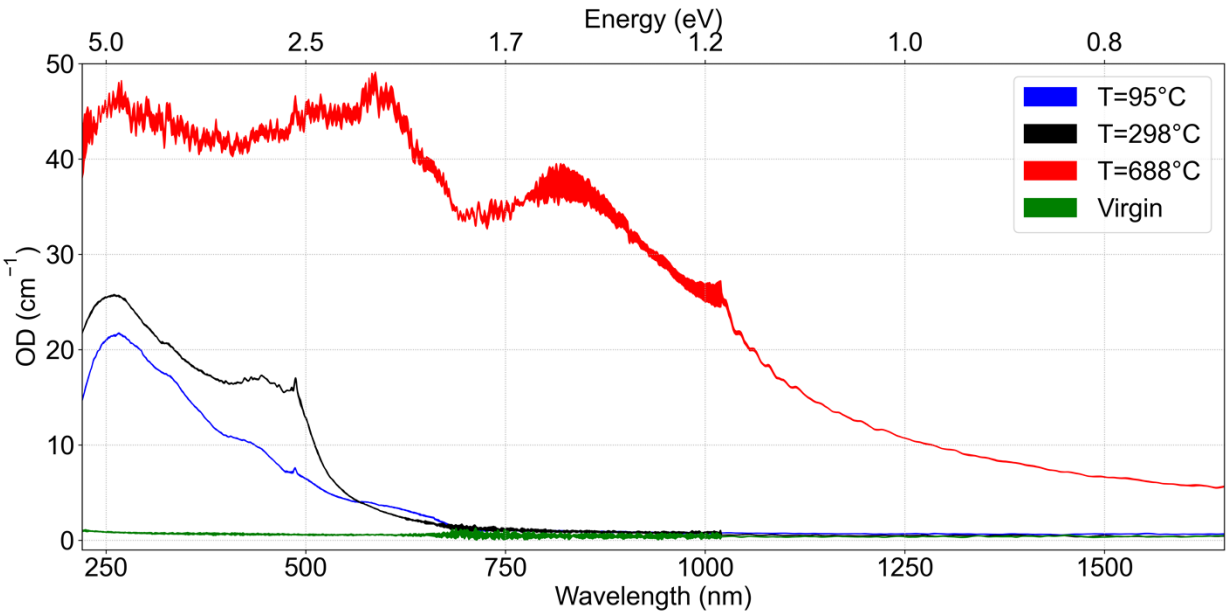

Figure 2. OD vs. photon wavelength for virgin and irradiated samples, with the irradiation temperature (T) as a parameter.

4. Discussion

4.1. Impact of impurity absorption

As mentioned previously, V, Cr, and Ti concentrations for all irradiated and virgin samples were indistinguishable from background within the experimental detection limits (~0.5 at%). Results from previous works can be used to estimate the approximate magnitude for the impurity concentrations that would be required to produce an OD that matches the OD spectra measured after irradiation. These concentrations can then be compared with the EDS detection limits. Moulton determined the effective cross section for the 490 nm Ti^{3+} absorption peak to be

~6.5 × 10^{-20} cm^2 or ~2.8 × 10^{-20} cm^2, depending on the polarization [85]. Ignoring the fact that there is no clear peak in the absorption spectra measured in this work, the measured OD in the range of 490 nm is ~45 cm^{-1}. Depending on which absorption cross section is used, this corresponds to a Ti^{3+} concentration of ~6.9 × 10^{20} cm^{-3} (5.5 at%) or ~1.6 × 10^{21} cm^{-3} (12.7 at%). Similarly, Govinda observed an ~10 cm^{-1} increase in absorption near 550 nm for sapphire samples with 2 at% of Cr compared to un-doped sapphire [84]. Therefore, the Cr impurity concentration would have to be on the order of 9 at% to cause ~45 cm^{-1} absorption. Finally, McClure measured the OD of sapphire samples doped with ~0.2 at% of V [83]. For both light polarizations, the maximum measured OD in the range of 300–700 nm was ~1 cm^{-1}. Therefore, the V impurity concentration would also have to be on the order of 9 at% to cause ~45 cm^{-1} absorption. Comparing these concentrations to the EDS detection limits (~0.5 at%), it is unlikely that the large increases in OD observed after irradiation at 688°C were caused by impurity absorption.

4.2. OD measurements compared to previous works

The OD measurements presented in Figure 2 are replotted in Figure 3 on a logarithmic scale so that they can be compared with previous measurements obtained after irradiation to orders-of-magnitude lower neutron fluences at a temperature of 77°C [58]. Measurements obtained during this work that were made after irradiation at 95 and 298°C are only shown for wavelengths up to 700 nm, which is the wavelength at which the OD was equal to that of the virgin sample within experimental uncertainties. The most obvious difference between all these data is that the OD measured after irradiation at 688°C is much larger and extends further into the infrared range. The hypothesized origins of the OD observed after the highest temperature irradiation are discussed below in Section 4.3.

The OD measured after irradiation at 95 and 298°C generally shows broader absorption peaks compared to those from Islamov after irradiation to much lower neutron fluences. Nevertheless, many of the absorption peaks identified by Islamov and found in earlier works are evident in the OD spectra reported herein after irradiation at 95 and 298°C. For example, the peak absorption in this work occurs near 250–260 nm, which has been attributed to the F^+ center, a positively charged oxygen vacancy [86, 87]. Although there are no specific peaks in the 300–350 nm range, there does appear to be a broad absorption band centered near 325 nm, which lies in between the 300 and 355 nm bands observed by Islamov [58]. These bands have been attributed to oxygen divacancies with a neutral and +1 charge, respectively [88, 89]. Islamov also observed a broad band near 450 nm [58], previously attributed to an oxygen divacancy with a +2 charge [88], and the present work may show evidence of a weak absorption band in this range after irradiation at 298°C. After irradiation at 95°C, the OD spectrum shows an inflection point closer to 400 nm, which is close to a known V center (413 nm), that has been postulated to be a composite of aluminum vacancy centers [87, 90, 91]. Therefore, while there are some differences in the spectral features of the OD observed in this work vs. those in Islamov's work, the general trends are similar, and many of the observed features can be explained by known defects that have been identified in the literature.

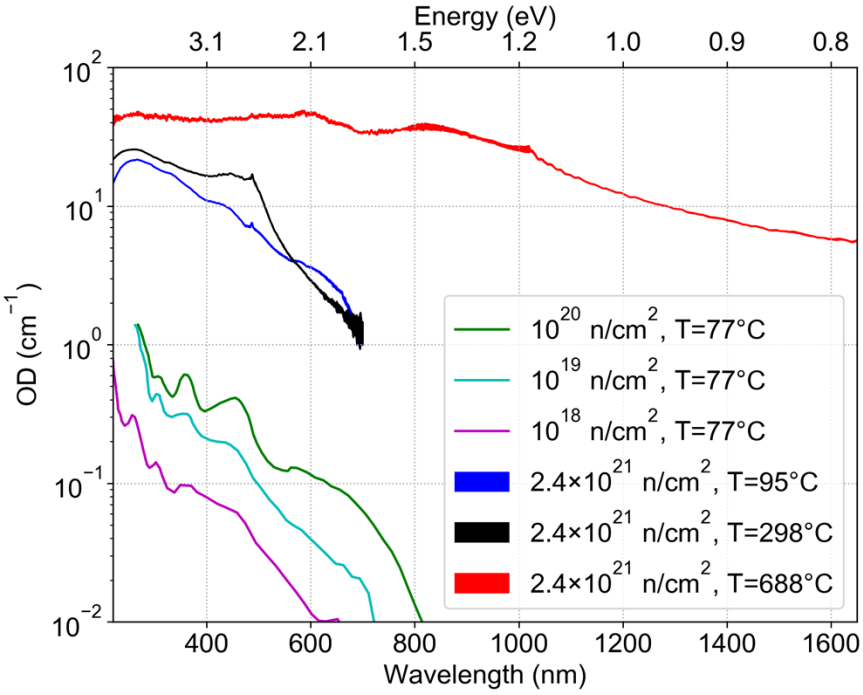

Figure 3. OD measured in this work (blue, black, red) compared to a previous work [58] that tested to lower neutron fluences at a temperature of 77°C. Measured OD values from this work after irradiation at 95 and 298°C are only shown for wavelengths for which the OD was statistically greater than that of the unirradiated sample.

The only previous work that evaluated the effects of temperature (beyond ~100°C) during neutron irradiation on the optical transmission of sapphire is the work by Petrie et al., in which sapphire fibers were interrogated in situ during neutron irradiation while the temperature was actively varied [49]. Petrie et al. observed linear increases in optical attenuation at 650 nm with increasing irradiation time and reported the time rate of change in this attenuation (Ȧ) as a function of temperature. Figure 4 shows normalized attenuation at 650 nm vs. irradiation temperature comparing OD data from this work (red) with the previous time rates of change in attenuation (blue). Data are normalized to values measured at the lowest irradiation temperature. The normalized attenuation shows reasonable agreement moving from the lowest temperature (56 or 95°C) to ~300°C. However, the previous work shows a significant reduction in attenuation

when the temperature is increased to 600°C or higher, in stark contrast to the present work, which shows an increase in attenuation by a factor of nearly 16. Clearly, the much lower fast neutron fluence in the previous work (6.9×10^{15} n/cm^2) resulted in significant differences in temperature trends.

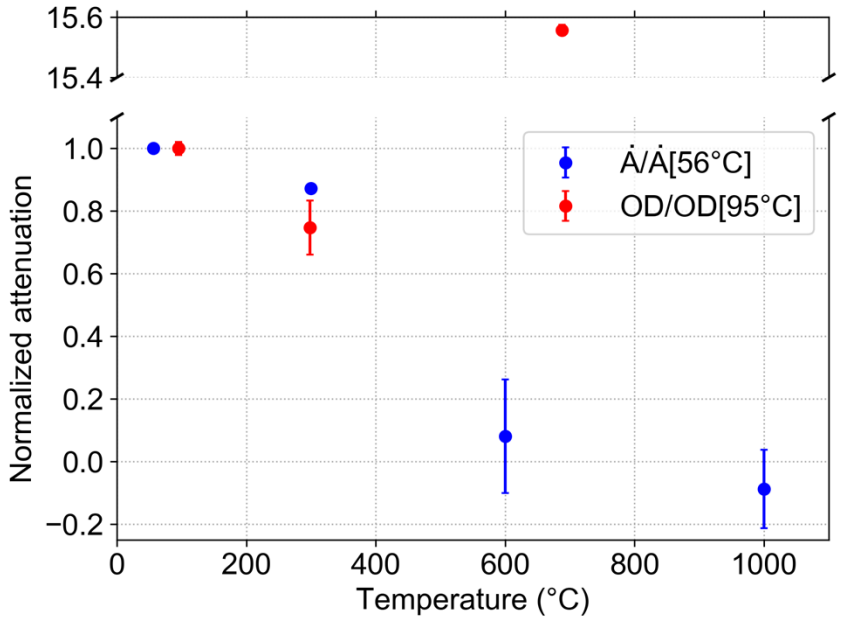

Figure 4. Normalized attenuation at 650 nm vs. irradiation temperature comparing OD data from this work (red) with previous in situ measurements of the time rates of change in attenuation (Ȧ, blue) during lower neutron flux irradiations [49]. Data are normalized to values measured at the lowest irradiation temperature.

4.3. Hypothesized origins of high-temperature radiation-induced optical absorption

The large increase in OD following irradiation at 688°C was not observed after lower temperature irradiations to the same neutron fluence (Figure 2) or after lower neutron fluence irradiation at similar temperatures [49]. Therefore, it appears that this phenomenon is caused by a combination of higher irradiation temperature and higher neutron fluence. Previous works have found that void formation in α-Al_2O_3 following neutron irradiation depends on both temperature and neutron fluence. Kinoshita et al. performed transmission electron microscopy to look for the

presence of voids in α-Al_2O_3 samples exposed to many different combinations of neutron fluence and temperature and produced a curve that predicts the threshold for void or cavity formation [69]. Kinoshita's data can be reasonably well fit ($R^2 = 0.964$) to give the following equation for the threshold temperature (T, ~650–1100 K or 377–827°C) required for void formation as a function of the neutron fluence (ϕ, ~10^{19}–10^{22} n/cm^2):

$$T[K] = 2.28 \times 10^7 \left\{ \phi \left[\frac{n}{cm^2} \right] \right\}^{-0.211}. \quad (2)$$

For the fast neutron fluence tested in this work (2.4×10^{21} n/cm^2), void formation would be expected when the irradiation temperature exceeds 410–420°C. Therefore, it is possible that the large increases in OD that were only observed following irradiation at 688°C, and not after irradiation at 95 and 298°C, are related to void formation. Clinard et al. performed transmission electron microscopy on α-Al_2O_3 samples irradiated at similar temperatures (652–827°C) at slightly higher neutron fluences (3×10^{21} to 2.1×10^{22} n/cm^2) and found voids aligned in rows along the c-axis with diameters ranging from 3.6 to 9 nm and spacing ranging from 7 to 21 nm [68]. Because these voids are small compared to the tested optical transmission wavelengths (220–1600 nm) and have a lower refractive index (unity) compared to the bulk material, they could cause significant Rayleigh scattering of light.

The spectral features of the OD can provide additional insights into whether Rayleigh scattering from voids formed at higher irradiation temperatures are responsible for the observed increases in OD. The spectral features following irradiation at 688°C are significantly different than those observed after irradiation at 95 and 298°C. Figure 2 shows a strong wavelength dependence of the OD, particularly in the range of 1100 to 1600 nm. It is well known that Rayleigh scattering losses following a λ^{-4} dependence [92]. Fitting the OD in the 1100 to 1600 nm range to λ^{-m} multiplied by a constant gives a value of m = 4.3 ($R^2 = 0.999$), which is within

10% of the theoretical value for Rayleigh scattering. The fact that the λ^{-4} trend does not continue for lower wavelengths could potentially be explained by coupling of scattered light from the sample back into the collection optics. At a low enough wavelength, the incident light could be scattered multiple times while passing through the specimen. At this point, the directionality of the scattered light would be more random and have a reduced dependence on wavelength. A small portion of the light escaping the specimen could be coupled back into the collection optics and contribute to the measured light intensities. Although transmission electron microscopy would be required to confirm the presence of voids, the spectral features of the attenuation provide additional evidence that void formation following higher temperature neutron irradiation of sapphire may be responsible for the large increases in OD.

4.4. Dimensional and lattice parameter measurements compared to previous works

Volumetric swelling in α-Al_2O_3 has been thoroughly investigated over a wide range of neutron fluence and temperature, particularly for polycrystalline α-Al_2O_3 [63, 68, 70-72, 93-98]. However, there are fewer data that report the crystallographic directional-dependence of radiation-induced dimensional changes in single-crystal sapphire as a function of fast neutron fluence and temperature. This crystallographic dependence is required to estimate drift of some single-crystal sapphire optical fiber–based interferometric sensors. Figure 5a shows both a-axis and c-axis macroscopic dimensional changes in single-crystal sapphire as a function of fast neutron fluence at various temperatures, including the a-axis measurements made in this effort and data that are available in the literature [70, 71, 74]. Figure 5b shows similar data for the a-axis and c-axis lattice expansion, including the present c-axis measurements as well as measurements from the literature [63, 74, 75, 97, 99].

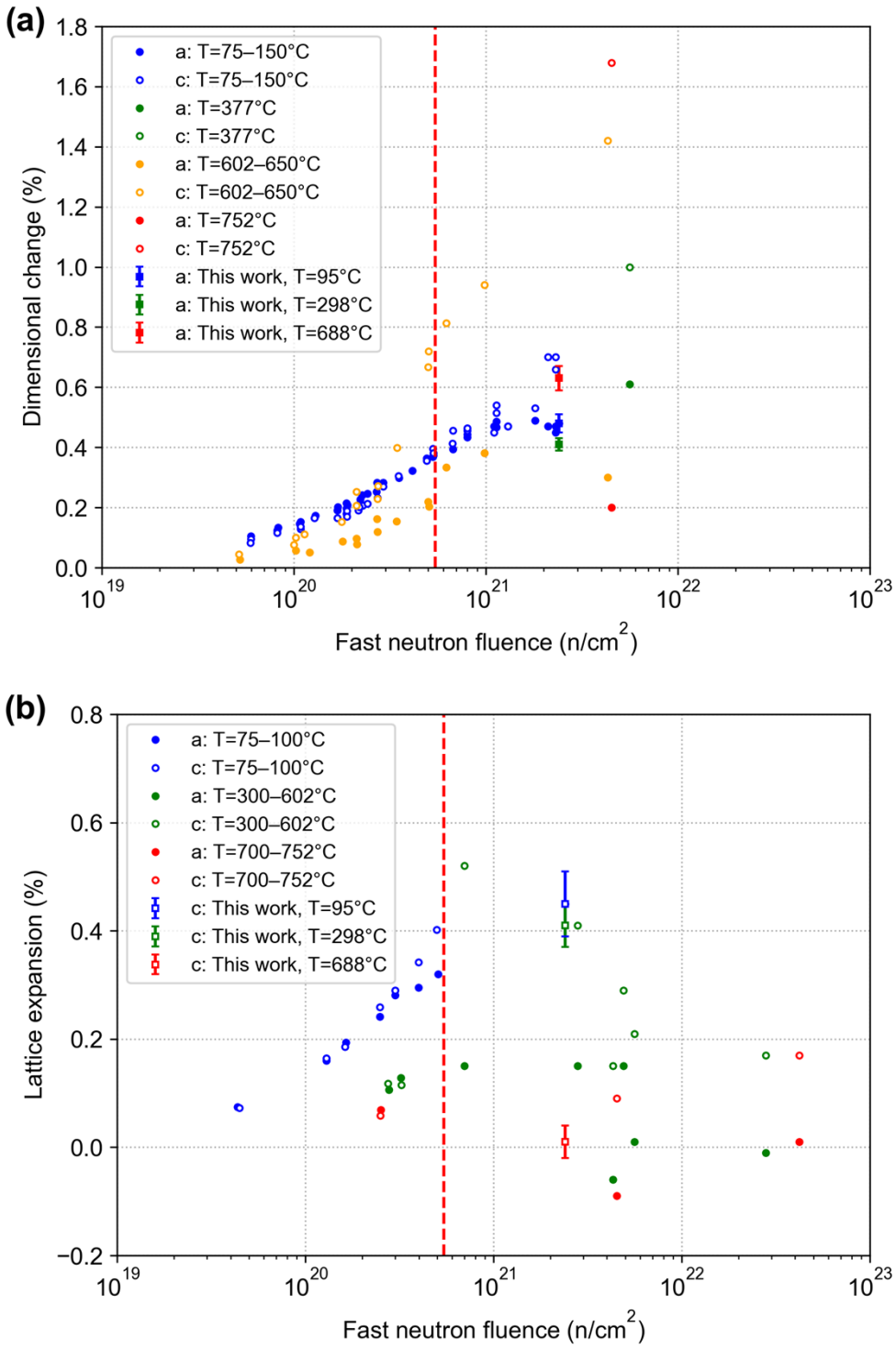

Figure 5. Measurements from this work compared with literature data for (a) macroscopic dimensional changes [70, 71, 74] and (b) lattice expansion [63, 74, 75, 97, 99] along the a- and c-axes vs. fast neutron fluence and temperature. The dashed red lines indicate the expected fluence at which void formation is expected during irradiation at 688°C based on Kinoshita's work [69].

The a-axis dimensional change measured in this work after irradiation at 95°C is consistent with previous measurements made after irradiation to lower neutron fluences at similar temperatures of 75–150°C. These data show some evidence of plateauing, although data at higher neutron fluence would be required to confirm this. Following irradiation at 298°C, the a-axis dimensional change (0.41%) is slightly lower compared to the value after irradiation at 95°C (0.48%). However, previous measurements showed significantly higher a-axis dimensional change (0.61%) following irradiation to 5.6×10^{21} n/cm^2 at 377°C [74], implying that a-axis dimensional changes may continue to increase beyond 2.4×10^{21} n/cm^2 for temperatures <400°C. After irradiation to 2.4×10^{21} n/cm^2 at 688°C, the a-axis dimensional change (0.63%) measured in this work is larger than previously reported values of 0.38% following irradiation to 9.8×10^{20} n/cm^2 at 650°C [70], and 0.3% following irradiation to 4.3×10^{21} n/cm^2 at 602°C [74]. More important for sapphire optical fibers is the c-axis dimensional change, which continues to increase at a higher rate compared to the a-axis with increasing neutron fluence for all irradiation temperatures. This increased anisotropic swelling can eventually result in grain boundary separation in polycrystalline materials [71, 75, 76].

Comparing Figure 5b with Figure 5a can provide some insights into whether lattice expansions are contributing significantly to the radiation-induced dimensional changes. The c-axis lattice expansion data reported in this work are generally consistent with previous measurements made at similar fast neutron fluences and temperatures. Figure 5b shows that lattice expansions are relatively small compared to the macroscopic dimensional changes except for measurements made following irradiation to fast neutron fluences less than ~10^{21} n/cm^2 at temperatures of 75–150°C. This is consistent with previous conclusions that high-dose macroscopic dimensional changes in α-Al_2O_3 are driven by larger defect clusters. The dashed red

lines in Figure 5 show the fast neutron fluence at which voids are expected to form during irradiation at 688°C according to Kinoshita's data (Equation 2) [69]. There is a significant increase in slope near this fluence in Wilks's c-axis dimensional change data (Figure 5a) at 650°C, whereas lattice expansion (Figure 5b) does not change significantly near this fluence. Therefore, it is likely that void formation plays a significant role in the c-axis dimensional changes observed in this temperature and neutron fluence regime.

4.5. Implications for in-core fiber-optic measurements

The optical absorption reported in this work increased significantly following exposure to a high neutron fluence of 2.4×10^{21} n/cm^2 at a temperature of 688°C vs. at lower irradiation temperatures (95 and 298°C). The lack of significant chemical impurities, the spectral features of the OD, and previous observations of voids following irradiation under similar conditions all point to Rayleigh scattering from radiation-induced voids as the mechanism for this large increase in OD. If this Rayleigh scattering is indeed responsible for the observed OD following irradiation at 688°C, then sapphire fiber–based sensors would have to be limited to fast neutron fluences below the threshold for void formation (Equation 2) to prevent these prohibitively large increases in attenuation. Future work could investigate the impact of rate effects on the threshold neutron fluence for void formation and whether this threshold could be higher for sapphire fibers irradiated under a lower fast neutron flux.

In addition to being impacted by increased optical attenuation, Bragg grating–based temperature or strain sensors in sapphire optical fibers may also be impacted by radiation-induced c-axis dimensional changes that cannot be distinguished from changes in temperature or strain. For single crystalline fibers, the volumetric swelling ($\frac{\Delta V}{V_0}$, Figure 1) is equal to

$$\frac{\Delta V}{V_0} = \frac{\Delta c}{c_0} + 2\frac{\Delta a}{a_0}, \quad (3)$$

where $\frac{\Delta c}{c_0}$ and $\frac{\Delta a}{a_0}$ are the changes in macroscopic c-axis and a-axis dimensions, respectively, relative to their pre-irradiation values (denoted with a zero subscript). A Bragg grating sensor inscribed in a sapphire fiber with the fiber's axis aligned along the c-axis would experience a relative shift in wavelength ($\frac{\Delta\lambda}{\lambda_0}$) equal to

$$\frac{\Delta\lambda}{\lambda_0} = \frac{\Delta c}{c_0} + \frac{\Delta n}{n_0}, \tag{4}$$

where $\frac{\Delta n}{n_0}$ is the relative change in refractive index $\Delta n = n - n_0$ relative to the value n_0 prior to irradiation.

The authors are unaware of any reported data regarding the change in refractive index for sapphire as a function of neutron fluence and irradiation temperature. However, to a first order, the Lorentz-Lorenz formula can be used to estimate changes in refractive index caused by volumetric swelling:

$$\frac{\Delta V}{V_0} + 1 = \frac{(n^2+2)(n_0^2-1)}{(n_0^2+2)(n^2-1)}. \tag{5}$$

Equations 3–5 can be solved for $\frac{\Delta\lambda}{\lambda_0}$ using the values for $\frac{\Delta a}{a_0}$ in this work (Table 1) and assuming $n_0 = 1.75$ near 1550 nm, which is a common wavelength for fiber Bragg gratings. For the 95°C $\frac{\Delta a}{a_0}$ data point, a value of $\frac{\Delta c}{c_0} = 0.70\%$ was used because this dimensional change was directly measured after irradiation to 2.3×10^{21} n/cm^2 at 75°C [71]. For the 298°C $\frac{\Delta a}{a_0}$ data point, a coarse approximation of $\frac{\Delta V}{V_0} = 1.69\%$ ($\frac{\Delta c}{c_0} = 0.87\%$ per Equation 3) was made by performing a neutron fluence-based interpolation between values in Figure 1 at 1.1×10^{21} n/cm^2 (150°C, $\frac{\Delta V}{V_0} = 1.5\%$

[70]) and 5.6 × 10^{21} n/cm^2 (377°C, $\frac{\Delta V}{V_0} = 2.2\%$ [73]), while ignoring the differences in temperature between the two data points. Considering that nearly all the previously reported swelling data in Figure 1 are between 1.5 and 2%, for neutron fluences between 1.1–4.3 × 10^{21} n/cm^2 and temperatures between 75–602°C, the uncertainty in this interpolated volumetric swelling value is likely in the range of 0.2%. For the 688°C $\frac{\Delta a}{a_0}$ data point, an approximate value of $\frac{\Delta c}{c_0} = 1.24\%$ was determined by performing a neutron fluence-based interpolation between values in Figure 5a at 9.8 × 10^{20} n/cm^2 (650°C, $\frac{\Delta c}{c_0} = 0.94\%$ [70]) and 4.5 × 10^{21} n/cm^2 (752°C, $\frac{\Delta c}{c_0} = 1.68\%$ [74]). Once again, the differences in temperature between the interpolation points were ignored. There is clearly a need for additional data regarding the directionally dependent dimensional changes in sapphire, as well as the changes in refractive index, as a function of irradiation temperature and neutron fluence. However, the data presented here provide at least an initial estimate for the trends in the expected drift in sapphire fiber–based temperature sensors as a function of irradiation temperature for a constant fast neutron fluence.

The calculated signal drift for Bragg gratings sensors as a function of irradiation temperature is summarized in Table 2. Values are shown for $\frac{\Delta\lambda}{\lambda_0}$ and the corresponding temperature drift (ΔT) using the thermal sensitivity of 25 pm °C^{-1} reported by Grobnic [42] for a Bragg grating centered near 1550 nm, corresponding to ~16 ppm °C^{-1}. In general, the decrease in refractive index has a larger effect on the drift compared to the c-axis swelling. Table 2 shows that the drift results in an apparent decrease in temperature that is as high as 139°C following irradiation at 95°C. Increasing the irradiation temperature from 95 to 298°C does not significantly change $\frac{\Delta V}{V_0}$ or $\frac{\Delta n}{n_0}$, but the increase in anisotropic swelling results in a higher value of

$\frac{\Delta c}{c_0}$ that is closer in magnitude to $\frac{\Delta n}{n_0}$, thus reducing the drift. Volumetric swelling in polycrystalline α-Al_2O_3 has been shown to have minimal temperature dependence in the range of 70 to 325°C following irradiation to fast neutron fluences of ~2.4×10^{21} n/cm^2 [76]. Increasing the irradiation temperature from 298 to 688°C increases the magnitude of $\frac{\Delta c}{c_0}$ and $\frac{\Delta n}{n_0}$, but the relative increase in $\frac{\Delta c}{c_0}$ is lower, causing a net increase in the calculated drift. This behavior illustrates the importance of quantifying the swelling anisotropy to determine the relative contributions to $\frac{\Delta c}{c_0}$ vs. $\frac{\Delta V}{V_0}$ (and consequently, $\frac{\Delta n}{n_0}$). For comparison, the drift in amorphous fused silica-based sensors after accumulating the same neutron fluence was calculated to be -103, -83, and -23°C at nominal temperatures of 95, 298, and 688°C, respectively [80].

Table 2. Summary of changes in dimensions ($\frac{\Delta a}{a_0}$ and $\frac{\Delta c}{c_0}$), volumetric swelling ($\frac{\Delta V}{V_0}$), and refractive index ($\frac{\Delta n}{n_0}$), as well as the calculated signal drift ($\frac{\Delta \lambda}{\lambda_0}$ and ΔT) in sapphire fiber–based Bragg grating temperature sensors after accumulating a fast neutron fluence of 2.4×10^{21} n/cm^2 at various irradiation temperatures.

Temperature (°C)	$\frac{\Delta a}{a_0}$	$\frac{\Delta c}{c_0}$	$\frac{\Delta V}{V_0}$	$\frac{\Delta n}{n_0}$	$\frac{\Delta \lambda}{\lambda_0}$	ΔT (°C)
95	0.48%	0.70%	1.66%	-0.92%	-0.22%	-139
298	0.41%	0.87%	1.69%	-0.94%	-0.07%	-43
688	0.63%	1.24%	2.50%	-1.37%	-0.13%	-83

5. Conclusions

This work presents optical absorption and directionally dependent dimensional measurements of single-crystal sapphire samples following irradiation to a high fast neutron fluence of 2.4×10^{21} n/cm^2 at temperatures of 95, 298, and 688°C. Following irradiation at 95 and 298°C, the spectral features of the optical absorption are similar (although with higher

magnitude) to those from earlier measurements [58] on samples irradiated at lower temperatures to an approximately order of magnitude lower neutron fluence. The change in optical absorption at 650 nm following irradiation at 298°C relative to that after irradiation at 95°C was also found to be generally consistent with a similar ratio (data at 300°C relative to that at 56°C) of the time rates of change in optical attenuation observed in situ during a previous neutron irradiation [49] at a far lower neutron flux. However, following irradiation at 688°C, the optical absorption increased dramatically and showed significantly different spectral features, which is in stark contrast to the prior in situ measurements at much lower neutron flux, which showed a significant reduction in the time rate of change in optical attenuation.

Spectral analyses of the OD following irradiation at 688°C showed a $\lambda^{-4.3}$ dependence from 1100–1600 nm, which is close to the expected λ^{-4} trend that is known for Rayleigh scattering losses. This, combined with previous observations of voids in this temperature and fluence regime [69], offers compelling evidence that Rayleigh scattering is responsible for the prohibitively large attenuation observed following irradiation at 688°C. Finally, analysis of the radiation-induced swelling reported here, and previously, predicts that swelling should result in a net negative drift in Bragg grating temperature sensors in sapphire optical fibers, because the reduction in refractive index is larger than the c-axis expansion. After accumulating a fast neutron fluence of 2.4×10^{21} n/cm^2, the calculated drift is as large as -139°C following irradiation at 95°C, and the magnitude of the drift varies with temperature according to the anisotropy in the radiation-induced dimensional changes. The observed optical attenuation and predicted signal drift pose serious questions regarding the use of sapphire fiber–based sensors for high-temperature, high-dose nuclear applications, particularly within the void swelling regime.

6. Acknowledgments

The initial conception and execution of the irradiation experiments presented herein were funded by the Laboratory Directed Research and Development Program of ORNL, managed by UT-Battelle, LLC, for the US Department of Energy (DOE). A portion of this research used the irradiation capabilities of HFIR, a DOE Office of Science User Facility operated by Oak Ridge National Laboratory (ORNL). Post-irradiation measurements were made using the ORNL Irradiated Materials Examination and Testing hot cell facility and the Low Activation Materials Development and Analysis (LAMDA) facility. The post-irradiation examination was supported by the DOE, Office of Nuclear Energy (DOE-NE) under DOE Idaho Operations Office Contract DE-AC07- 051D14517 as part of a Nuclear Science User Facilities experiment. Curation and analysis of the post-irradiation measurement data was supported by the Nuclear Energy Enabling Technologies Program of DOE-NE. Jesse Werden, Alicia Raftery, and Kory Linton assisted in coordination of the post-irradiation examination. Travis Dixon performed the sample exchanges during the optical transmission measurements in LAMDA, and Keyou Mao performed the EDS measurements. Matt Kurley and Ercan Cakmak performed the XRD measurements. Adrian Schrell and Brandon Wilson provided helpful comments on the manuscript.

7. References

[1] C.R. McCullough, Summary report on design and development of high temperature gas-cooled power pile, Clinton Labs, Oak Ridge, TN, 1947.
[2] J.L. Everett, E.J. Kohler, Peach Bottom unit no. 1: A high performance helium cooled nuclear power plant, Annals of Nuclear Energy 5(8) (1978) 321–335.
[3] A.L. Habush, A.M. Harris, 330-MW(e) Fort St. Vrain high-temperature gas-cooled reactor, Nucl. Eng. Des. 7(4) (1968) 312–321.
[4] R.C. Briant, A.M. Weinberg, Molten Fluorides as Power Reactor Fuels, Nucl. Sci. Eng. 2(6) (1957) 797–803.
[5] P.N. Haubenreich, J.R. Engel, Experience with the Molten-Salt Reactor Experiment, Nuclear Applications and Technology 8(2) (1970) 118–136.
[6] S.J. Zinkle, G.S. Was, Materials challenges in nuclear energy, Acta Materialia 61(3) (2013) 735–758.

[7] H.M. Hashemian, On-line monitoring applications in nuclear power plants, Progress in Nuclear Energy 53(2) (2011) 167–181.
[8] K. Korsah, R. Kisner, C. Britton Jr., P. Ramuhalli, D.W. Wootan, N.C. Anheier, A.A. Diaz, E.H. Hirt, R. Vilim, H.-T. Chien, Assessment of sensor technologies for advanced reactors, Oak Ridge National Laboratory, Oak Ridge, TN, 2017.
[9] C.M. Petrie, A.M. Schrell, D.N. Leonard, Y. Yang, B.C. Jolly, K.A. Terrani, Embedded sensors in additively manufactured silicon carbide, J. Nucl. Mater. 552 (2021) 153012.
[10] D.C. Crawford, D.L. Porter, S.L. Hayes, M.K. Meyer, D.A. Petti, K. Pasamehmetoglu, An approach to fuel development and qualification, J. Nucl. Mater. 371(1) (2007) 232–242.
[11] B.G. Kim, J.L. Rempe, J.-F. Villard, S. Solstad, Review Paper: Review of Instrumentation for Irradiation Testing of Nuclear Fuels and Materials, Nucl. Technol. 176(2) (2011) 155–187.
[12] S. Solstad, R. Van Nieuwenhove, Instrument Capabilities and Developments at the Halden Reactor Project, Nucl. Technol. 173(1) (2011) 78–85.
[13] G.B. Hocker, Fiber-optic sensing of pressure and temperature, Appl. Opt. 18(9) (1979) 1445–1448.
[14] J.N. Fields, C.K. Asawa, O.G. Ramer, M.K. Barnoski, Fiber optic pressure sensor, The Journal of the Acoustical Society of America 67(3) (1980) 816–818.
[15] Y. Zhu, A. Wang, Miniature fiber-optic pressure sensor, IEEE Photonics Technology Letters 17(2) (2005) 447–449.
[16] J.X. Fang, H.F. Taylor, H.S. Choi, Fiber-optic Fabry–Perot flow sensor, Microwave and Optical Technology Letters 18(3) (1998) 209–211.
[17] T. Chen, Q. Wang, B. Zhang, R. Chen, K.P. Chen, Distributed flow sensing using optical hot-wire grid, Opt. Express 20(8) (2012) 8240–8249.
[18] R. Chen, A. Yan, Q. Wang, K.P. Chen, Fiber-optic flow sensors for high-temperature environment operation up to 800°C, Opt. Lett. 39(13) (2014) 3966–3969.
[19] C.M. Petrie, J.L. McDuffee, Liquid level sensing for harsh environment applications using distributed fiber optic temperature measurements, Sensors and Actuators A: Physical 282 (2018) 114–123.
[20] P. Raatikainen, I. Kassamakov, R. Kakanakov, M. Luukkala, Fiber-optic liquid-level sensor, Sensors and Actuators A: Physical 58(2) (1997) 93–97.
[21] A. Wang, M.F. Gunther, K.A. Murphy, R.O. Claus, Fiber-optic liquid-level sensor, Sensors and Actuators A: Physical 35(2) (1992) 161–164.
[22] M. Bliss, R.L. Brodzinski, R.A. Craig, B.D. Geelhood, M.A. Knopf, H.S. Miley, R.W. Perkins, P.L. Reeder, D.S. Sunberg, R.A. Warner, N.A. Wogman, Glass-fiber-based neutron detectors for high- and low-flux environments, SPIE's 1995 International Symposium on Optical Science, Engineering, and Instrumentation, SPIE, San Diego, CA, 1995.
[23] G.A. Wurden, R.E. Chrien, C.W. Barnes, W.C. Sailor, A.L. Roquemore, M.J. Lavelle, P.M. O'Gara, R.J. Jordan, Scintillating-fiber 14 MeV neutron detector on TFTR during DT operation, Rev. Sci. Instrum. 66(1) (1995) 901–903.
[24] B. Brichard, A.F. Fernandez, H. Ooms, F. Berghmans, Fibre-optic gamma-flux monitoring in a fission reactor by means of Cerenkov radiation, Measurement Science and Technology 18(10) (2007) 3257–3262.
[25] T.W. Wood, B. Blake, T.E. Blue, C.M. Petrie, D. Hawn, Evaluation of the Performance of Distributed Temperature Measurements with Single-Mode Fiber Using Rayleigh Backscatter up to 1000°C, IEEE Sens. J. 14(1) (2014) 124–128.

[26] D.C. Sweeney, A.M. Schrell, C.M. Petrie, An Adaptive Reference Scheme to Extend the Functional Range of Optical Backscatter Reflectometry in Extreme Environments, IEEE Sens. J. 21(1) (2020) 498–509.
[27] D. Grobnic, C.W. Smelser, S.J. Mihailov, R.B. Walker, Long-term thermal stability tests at 1000 °C of silica fibre Bragg gratings made with ultrafast laser radiation, Measurement Science and Technology 17(5) (2006) 1009.
[28] C.M. Petrie, N. Sridharan, M. Subramanian, A. Hehr, M. Norfolk, J. Sheridan, Embedded metallized optical fibers for high temperature applications, Smart Mater. Struct. 28 (2019) 055012.
[29] C.M. Petrie, N. Sridharan, In situ measurement of phase transformations and residual stress evolution during welding using spatially distributed fiber-optic strain sensors, Measurement Science and Technology 31(12) (2020) 125602.
[30] C.M. Petrie, N. Sridharan, A. Hehr, M. Norfolk, J. Sheridan, High-temperature strain monitoring of stainless steel using fiber optics embedded in ultrasonically consolidated nickel layers, Smart Mater. Struct. 28(8) (2019) 085041.
[31] A.H. Rose, Devitrification in annealed optical fiber, J. Lightw. Technol. 15(5) (1997) 808–814.
[32] R.K. Nubling, J.A. Harrington, Optical properties of single-crystal sapphire fibers, Appl. Opt. 36(24) (1997) 5934–5940.
[33] C.A. Burrus, L.A. Coldren, Growth of single-crystal sapphire-clad ruby fibers, Applied Physics Letters 31(6) (1977) 383–384.
[34] V.N. Kurlov, S.N. Rossolenko, S.V. Belenko, Growth of sapphire core-doped fibers, Journal of Crystal Growth 191(3) (1998) 520–524.
[35] C.-M. Liu, J.-C. Chen, C.-H. Chiang, L.-J. Hu, S.-P. Lin, Mg-Doped Sapphire Crystal Fibers Grown by Laser-Heated Pedestal Growth Method, Japanese Journal of Applied Physics 45(1A) (2006) 194–199.
[36] B.A. Wilson, T.E. Blue, Creation of an Internal Cladding in Sapphire Optical Fiber Using the Li-6 (n,alpha) H-3 Reaction, IEEE Sens. J. 17(22) (2017) 7433–7439.
[37] W.T. Spratt, M. Huang, C. Jia, L. Wang, V.K. Kamineni, A.C. Diebold, H. Xia, Formation of optical barriers with excellent thermal stability in single-crystal sapphire by hydrogen ion implantation and thermal annealing, Applied Physics Letters 99(11) (2011) 111909.
[38] S. Desu, R. Claus, R. Raheem, K. Murphy, High-temperature sapphire optical sensor fiber coatings, SPIE1990.
[39] A. Raheem-Kizchery, S. Desu, R. Claus, High Temperature Refractory Coating Materials For Sapphire Waveguides, SPIE1990.
[40] C.M. Petrie, T.E. Blue, In Situ Thermally Induced Attenuation in Sapphire Optical Fibers Heated to 1400°C, J. Am. Ceram. Soc. 98(2) (2015) 483–489.
[41] B.A. Wilson, C.M. Petrie, T.E. Blue, High-temperature effects on the light transmission through sapphire optical fiber, J. Am. Ceram. Soc. 101(8) (2018) 3452–3459.
[42] D. Grobnic, S.J. Mihailov, C.W. Smelser, D. Huimin, Sapphire fiber Bragg grating sensor made using femtosecond laser radiation for ultrahigh temperature applications, IEEE Photonics Technology Letters 16(11) (2004) 2505–2507.
[43] S. Yang, D. Hu, A. Wang, Point-by-point fabrication and characterization of sapphire fiber Bragg gratings, Opt. Lett. 42(20) (2017) 4219–4222.

[44] M. Busch, W. Ecke, I. Latka, D. Fischer, R. Willsch, H. Bartelt, Inscription and characterization of Bragg gratings in single-crystal sapphire optical fibres for high-temperature sensor applications, Measurement Science and Technology 20(11) (2009) 115301.
[45] B.A. Wilson, T.E. Blue, Quasi-Distributed Temperature Sensing Using Type-II Fiber Bragg Gratings in Sapphire Optical Fiber to Temperatures up to 1300°C, IEEE Sens. J. 18(20) (2018) 8345–8351.
[46] D. Sporea, A. Sporea, Radiation effects in sapphire optical fibers, physica status solidi c 4(3) (2007) 1356–1359.
[47] C.M. Petrie, B. Wilson, T.E. Blue, In Situ Gamma Radiation-Induced Attenuation in Sapphire Optical Fibers Heated to 1000°C, J. Am. Ceram. Soc. 97(10) (2014) 3150–3156.
[48] C.M. Petrie, W. Windl, T.E. Blue, In-Situ Reactor Radiation-Induced Attenuation in Sapphire Optical Fibers, J. Am. Ceram. Soc. 97(12) (2014) 3883–3889.
[49] C.M. Petrie, T.E. Blue, In situ reactor radiation-induced attenuation in sapphire optical fibers heated up to 1000 °C, Nucl. Instr. Meth. Phys. Res. B 342 (2015) 91–97.
[50] C.M. Petrie, Characterization of the Performance of Sapphire Optical Fiber in Intense Radiation Fields, when Subjected to Very High Temperatures, The Ohio State University, Columbus, OH, 2014.
[51] M. Okada, K. Atobe, M. Nakagawa, Irradiation temperature dependence of production efficiency of lattice defects in some neutron-irradiated oxides, Nucl. Instr. Meth. Phys. Res. B 226(3) (2004) 369–375.
[52] P.W. Levy, Color Centers and Radiation-Induced Defects in Al2O3, Physical Review 123(4) (1961) 1226–1233.
[53] B. Evans, H. Hendricks, F. Bazzarre, J. Bunch, Association of the 6-eV Optical Band in Sapphire with Oxygen Vacancies, Ion Implantation in Semiconductors 1976, Springer1977, pp. 265-274.
[54] B.D. Evans, A review of the optical properties of anion lattice vacancies, and electrical conduction in α-Al2O3: their relation to radiation-induced electrical degradation, J. Nucl. Mater. 219 (1995) 202-223.
[55] P.W. Levy, Annealing of the defects and colour centres in unirradiated and in reactor irradiated Al 2 O 3, Discussions of the Faraday Society 31 (1961) 118-129.
[56] M. Izerrouken, T. Benyahia, Absorption and photoluminescence study of Al2O3 single crystal irradiated with fast neutrons, Nucl. Instr. Meth. Phys. Res. B 268(19) (2010) 2987–2990.
[57] J.M. Bunch, F.W. Clinard Jr, Damage of Single-Crystal Al2O3 by 14-MeV Neutrons, J. Am. Ceram. Soc. 57(6) (1974) 279-280.
[58] A.K. Islamov, E.M. Ibragimova, I. Nuritdinov, Radiation-optical characteristics of quartz glass and sapphire, J. Nucl. Mater. 362(2) (2007) 222–226.
[59] M.F. Zhang, H.L. Zhang, J.C. Han, H.X. Guo, C.H. Xu, G.B. Ying, H.T. Shen, N.N. Song, Effects of neutron irradiation and subsequent annealing on the optical characteristics of sapphire, Physica B: Condensed Matter 406(3) (2011) 494–497.
[60] I.K. Abdukadyrova, Generation and annealing of radiational defects in neutron irradiated Al 2 O 3, Soviet Atomic Energy 62(3) (1987) 221-225.
[61] G. Pells, Colour centres in α-Al 2 O 3 and their application to fast neutron dosimetry, Radiation Physics and Chemistry 22(6) (1983) 1053-1056.
[62] S. Zinkle, Radiation-induced effects on microstructure, in: R. Konings, R. Stoller (Eds.), Comprehensive nuclear materials, Elsevier, Amsterdam, Netherlands, 2012, pp. 65-98.

[63] B. Hickman, D. Walker, The effect of neutron irradiation on aluminium oxide, J. Nucl. Mater. 18(2) (1966) 197–205.
[64] W.E. Lee, M.L. Jenkins, G.P. Pells, The influence of helium doping on the damage microstructure of heavy-ion irradiated α-Al2O3, Philosophical Magazine A 51(5) (1985) 639-659.
[65] M. Akiyoshi, N. Akasaka, Y. Tachi, T. Yano, Relation between macroscopic length change and the crystal structure in heavily neutron-irradiated ceramics, J. Nucl. Mater. 329-333 (2004) 1466-1470.
[66] D.G. Howitt, T.E. Mitchell, Electron irradiation damage in a-Al2O3, Philosophical Magazine A 44(1) (1981) 229-238.
[67] G.P. Pells, Radiation Damage Effects in Alumina, J. Am. Ceram. Soc. 77(2) (1994) 368–377.
[68] F.W. Clinard, G.F. Hurley, L.W. Hobbs, Neutron irradiation damage in MgO, Al2O3 and MgAl2O4 ceramics, J. Nucl. Mater. 108-109 (1982) 655–670.
[69] C. Kinoshita, S.J. Zinkle, Potential and limitations of ceramics in terms of structural and electrical integrity in fusion environments, J. Nucl. Mater. 233-237 (1996) 100-110.
[70] R. Wilks, J. Desport, J. Smith, The irradiation-induced macroscopic growth of α-Al2O3 single crystals, J. Nucl. Mater. 24(1) (1967) 80–86.
[71] G. Keilholtz, R. Moore, H. Robertson, Effects of fast neutrons on polycrystalline alumina and other electrical insulators at temperatures from 60° to 1230°C, Oak Ridge National Laboratory, Oak Ridge, TN, 1971.
[72] F. Clinard Jr, G. Hurley, L. Hobbs, D. Rohr, R. Youngman, Structural performance of ceramics in a high-fluence fusion environment, J. Nucl. Mater. 123(1-3) (1984) 1386–1392.
[73] F.W. Clinard, J.M. Bunch, W.A. Ranken, Neutron Irradiation Damage in Al2O3 and Y2O3, in: J.S. Watson, F.W. Wiffen (Eds.) Proceedings of the International Conference on Radiation Effects and Tritium Technology for Fusion Reactors, Gatlinburg, TN, 1976, p. 498.
[74] R.B. Roof, W.A. Ranken, Radiation effects on the lattice constants of single crystal A12O3, J. Nucl. Mater. 55(3) (1975) 357-358.
[75] G.W. Keilholtz, R.E. Moore, Irradiation Damage to Aluminum Oxide Exposed to 5 × 1021 Fast Neutrons/CM2, Nuclear Applications 3(11) (1967) 686-691.
[76] G.W. Keilholtz, R.E. Moore, H.E. Robertson, Fast-Neutron Damage to Polycrystalline Alumina at Temperatures from 60 to 1230°C, Nucl. Technol. 17(3) (1973) 234-246.
[77] R.D. Cheverton, T.M. Sims, HFIR Core Nuclear Design, Oak Ridge National Laboratory, Oak Ridge, TN, 1971.
[78] N. Xoubi, R.T. Primm III, Modeling of the High Flux Isotope Reactor Cycle 400, Oak Ridge, TN, 2005.
[79] S.J. Zinkle, C. Kinoshita, Defect production in ceramics, J. Nucl. Mater. 251 (1997) 200–217.
[80] C.M. Petrie, A. Birri, T.E. Blue, High-dose temperature-dependent neutron irradiation effects on the optical transmission and dimensional stability of amorphous fused silica, J. Non-Cryst. Solids 525 (2019) 119668.
[81] K.G. Field, J.L. McDuffee, J.W. Geringer, C.M. Petrie, Y. Katoh, Evaluation of the continuous dilatometer method of silicon carbide thermometry for passive irradiation temperature determination, Nucl. Instr. Meth. Phys. Res. B 445 (2019) 46–56.
[82] M. Villedieu, N. Devismes, A.M. de Goër, A study of valency changes of vanadium ions in Al2O3 by γ irradiation, Journal of Physics and Chemistry of Solids 38(9) (1977) 1063–1070.

[83] D.S. McClure, Optical spectra of transition-metal ions in corundum, The Journal of Chemical Physics 36(10) (1962) 2757–2779.
[84] S. Govinda, Coloration and luminescence in pure and chromium-doped Al2O3 single crystals irradiated with X-rays at room temperature, physica status solidi (a) 37(1) (1976) 109–117.
[85] P.F. Moulton, Spectroscopic and laser characteristics of Ti:Al2O3, JOSA B 3(1) (1986) 125–133.
[86] K.H. Lee, J.H. Crawford, Electron centers in single-crystal Al2O3, Physical Review B 15(8) (1977) 4065-4070.
[87] B.D. Evans, M. Stapelbroek, Optical properties of the F+ center in crystalline Al2O3, Physical Review B 18(12) (1978) 7089-7098.
[88] G. Pogatshnik, Y. Chen, B. Evans, A model of lattice defects in sapphire, IEEE Trans. Nucl. Sci. 34(6) (1987) 1709–1712.
[89] S.V. Solov'ev, I.I. Milman, A.I. Syurdo, Thermal- and photo-induced transformations of luminescence centers in αd-Al2O3 anion-defective crystals, Physics of the Solid State 54(4) (2012) 726-734.
[90] T. Turner, J. Crawford Jr, V centers in single crystal Al2O3, Solid State Communications 17(2) (1975) 167–169.
[91] B.D. Evans, L.S. Cain, A cation vacancy center in crystalline Al2O3, Radiation Effects and Defects in Solids 134(1-4) (1995) 329-332.
[92] A. Sa'ar, A. Katzir, Scattering effects in crystalline infrared fibers, J. Opt. Soc. Am. A 5(6) (1988) 823-833.
[93] R. Konings, K. Bakker, J. Boshoven, R. Conrad, H. Hein, The influence of neutron irradiation on the microstructure of Al2O3, MgAl2O4, Y3Al5O12 and CeO2, J. Nucl. Mater. 254(2-3) (1998) 135–142.
[94] D. Tucker, T. Zocco, C. Kise, J. Kennedy, Effects of neutron-irradiation on MgAl2O4 and Al2O3, J. Nucl. Mater. 141 (1986) 401–404.
[95] R. Youngman, T. Mitchell, F. Clinard, G. Hurley, High dose neutron irradiation damage in alpha alumina, Journal of materials research 6(10) (1991) 2178–2187.
[96] E. Neeft, R. Konings, K. Bakker, J. Boshoven, H. Hein, R. Schram, A. Van Veen, R. Conrad, Neutron irradiation of polycrystalline yttrium aluminate garnet, magnesium aluminate spinel and α-alumina, J. Nucl. Mater. 274(1-2) (1999) 78–83.
[97] T. Yano, K. Ichikawa, M. Akiyoshi, Y. Tachi, Neutron irradiation damage in aluminum oxide and nitride ceramics up to a fluence of 4.2× 1026n/m2, J. Nucl. Mater. 283 (2000) 947–951.
[98] M. Akiyoshi, T. Yano, Neutron-irradiation effect in ceramics evaluated from macroscopic property changes in as-irradiated and annealed specimens, Progress in Nuclear Energy 50(2-6) (2008) 567–574.
[99] R.S. Wilks, Neutron-induced damage in BeO, Al2O3 and MgO — a review, J. Nucl. Mater. 26(2) (1968) 137-173.